Acta Pharmaceutica Sinica B 2018;8(6):956–968

Chinese Pharmaceutical Association
Institute of Materia Medica, Chinese Academy of Medical Sciences

Acta Pharmaceutica Sinica B

www.elsevier.com/locate/apsb
www.sciencedirect.com

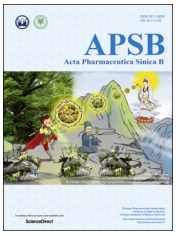

ORIGINAL ARTICLE

Tat-functionalized Ag-Fe_3O_4 nano-composites as tissue-penetrating vehicles for tumor magnetic targeting and drug delivery

Ergang Liu[a,b,c], Meng Zhang[c], Hui Cui[b], Junbo Gong[a], Yongzhuo Huang[c], Jianxin Wang[d], Yanna Cui[c], Weibing Dong[a], Lu Sun[b], Huining He[b,*], Victor C. Yang[a,b,e,*]

[a]*State Key Laboratory of Chemical Engineering, School of Chemical Engineering and Technology, Tianjin University, Tianjin 300072, China*
[b]*Tianjin Key Laboratory on Technologies Enabling Development of Clinical Therapeutics and Diagnosis, School of Pharmacy, Tianjin Medical University, Tianjin 300070, China*
[c]*Shanghai Institute of Materia Medica, Chinese Academy of Sciences, Shanghai 201203, China*
[d]*Department of Pharmaceutics, School of Pharmacy, Fudan University & Key Laboratory of Smart Drug Delivery, Ministry of Education, Shanghai 201203, China*
[e]*Department of Pharmaceutical Sciences, College of Pharmacy, University of Michigan, Ann Arbor, MI 48109-1065, USA*

Received 11 March 2018; received in revised form 19 April 2018; accepted 26 June 2018

KEY WORDS

Cell penetrating peptide;
Tat;
Silver nanoparticles;
Magnetic targeting;
Fe_3O_4;
Hydrazone bond

Abstract In this paper, we prepared a dual functional system based on dextrin-coated silver nanoparticles which were further attached with iron oxide nanoparticles and cell penetrating peptide (Tat), producing Tat-modified Ag-Fe_3O_4 nanocomposites (Tat-FeAgNPs). To load drugs, an –SH containing linker, 3-mercaptopropanohydrazide, was designed and synthesized. It enabled the silver carriers to load and release doxorubicin (Dox) in a pH-sensitive pattern. The delivery efficiency of this system was assessed *in vitro* using MCF-7 cells, and *in vivo* using null BalB/c mice bearing MCF-7 xenograft tumors. Our results demonstrated that both Tat and externally applied magnetic field could promote cellular uptake and consequently the cytotoxicity of doxorubicin-loaded nanoparticles, with the IC_{50} of Tat-FeAgNP-Dox to be 0.63 μmol/L. The *in vivo* delivery efficiency of Tat-FeAgNP carrying Cy5 to the mouse tumor was analyzed using the *in vivo* optical imaging tests, in which Tat-FeAgNP-Cy5 yielded the most efficient accumulation in the tumor (6.7 ± 2.4% ID of Tat-FeAgNPs). Anti-tumor assessment also demonstrated that Tat-FeAgNP-Dox displayed the most significant tumor-inhibiting effects and reduced the specific growth rate of tumor by 29.6% ($P = 0.009$), which

*Corresponding authors. Tel./fax: +86 22 83336658.
E-mail addresses: hehuining@tmu.edu.cn (Huining He), vcyang@med.umich.edu (Victor C. Yang).
Peer review under responsibility of Institute of Materia Medica, Chinese Academy of Medical Sciences and Chinese Pharmaceutical Association.

https://doi.org/10.1016/j.apsb.2018.07.012

could be attributed to its superior performance in tumor drug delivery in comparison with the control nanovehicles.

1. Introduction

It has been 31 years since Maeda and co-workers first published their reports on enhanced permeability and retention (EPR) effect, demonstrating that nano-sized macromolecules can pass through the leaky neo-vascular walls and accumulate in the tumor[1]. Maeda's findings reveal that nano-sized material can potentially alter small molecular drug's bio-distribution and improve therapeutic efficacy, and thus has attracted extensive attention in tumor chemotherapies. Inspired by this, we have witnessed great achievements made in nanomaterial-mediated cancer drug delivery during the past 30 years[2]. Up to now, the pool of cancer nanomedicine has collected thousands of nanomaterials ranged from naturally originated proteins[3], polysaccharides[4], to varied forms of synthetic polymers[5]. At the same time, the "targeting strategy" is also being updated from the initial "passive targeting" *via* EPR effect, to more sophisticated "active targeting" involving antibody or tumor specific ligand binding[6]. However, with respect to the quantities of tumor targeted nanomaterials, few of them have achieved a substantially efficient tumor accumulation[7,8]. Of note, it has been estimated that only 0.7% (median) of the administrated nano-materials were delivered to the solid tumors[8], making it an unconvincing slogan for the so-called targeted delivery.

Generally, the dilemma in tumor drug delivery may find its basis in anatomic features of human body. In order to achieve high efficient delivery, nanomaterials should be able to facilitate efficient tumor engulfment and at the same time be resistant to seizure by other organs. Unfortunately, neither of which has been well resolved thus far. The leakage tumor vasculatures have opened gates for nano-sized entities, yet the existence of membrane barriers, as well as hyper-interstitial pressure, prevents the vehicles from further permeation from vessels[9], thus limiting an efficient tumor uptake of the nanomaterials. In addition, non-selective uptake by tissues/organs takes up the main stream of cardiac output. Moreover, RES (reticuloendothelial system) organs such as liver, and spleen are featured in fenestrated endothelium and local lymphatic cells, and thus are capable of capturing the bypassed nano-materials. Therefore, it is not surprising why most of the "tumor-targeting" nanomaterials have yielded limited on-site delivery[10]. To this regard, it is now a fashioned strategy for "active targeting", *i.e.*, by taking advantage of tumor overexpressed proteins to increase the targeting efficiency. However, antibody or receptor binding still relies on the EPR effect, because the surface-modified nanomaterials have to extravasate from the vessels before the specific bindings occur[10]. As a result, though antibody/ligand modifications can promote the tumor retention and improve therapeutic efficacy at certain instances, the overall improvement on delivery efficiency is negligible because of limited tumor blood bypass[7].

Considering the main drawbacks of conventional tumor drug delivery systems are attributed to the inefficient EPR effect and tumor barriers, it is reasonable to assume that functionalization of the nanovehicle with improved EPR effect and accelerated tumor intake should yield a significant improvement in the overall delivery efficiency. Fig. 1 portrays our specially designed delivery system. In brief, the system is built with silver nanoparticles (AgNPs) as both anti-tumor agent[11] and convenient carrier because of the anti-bacterial effect of the released silver irons and its high affinity to sulfydryl group which enables an ease click-and-loading mechanism for thiolated drugs and functional moieties. The silver carriers are then subjected to a two-step modification to obtain the dual functions. Firstly, silver nanoparticles are crosslinked with iron oxide nanoparticles (Fe_3O_4NPs) to produce Ag-Fe_3O_4 nanocomposites (FeAgNPs). As a whole, the superparamagnetic part of Fe_3O_4NPs will grant the nanocomposites to be magnetized under magnetic field, thus producing a preferential magnetic moment that can be finely tuned against circulation shearing force and the hyper-interstitial pressure of tumor[12,13], both of which are assumed to further enhance the permeation and retention of the nano-composites. Secondly, FeAgNPs then are modified with thiolated cell penetrating peptide (CPP), Tat, through the –SH linkages, yielding the dual functionalized Tat-FeAgNPs. As known, Tat is derived from the transduction domain of HIV-1 Tat protein and has been proven to function as a penetration enhancer in delivering various cargos across the cell membrane barriers[14,15]. Herein, Tat is utilized to promote blood vessel penetration and intracellular uptake by the tumor. Compounding together, the whole system is proposed to function in a two-step process: once entering the systemic circulation, the nano-vehicles will be driven out of circulation and led to the tumor region by the localized magnetic field, whereas the surface-modified CPPs will then work to facilitate efficient tumor intracellular uptake. Since the system is specially designed to overcome the deficiencies associated with EPR effect, a substantially improved targeting efficiency of the delivered cargoes will therefore be warranted.

2. Materials and methods

2.1. Materials

Silver nitrate, ferric chloride hexahydrate, ferrous sulfate heptahydrate, dextrin, nitric acid, hydrogen peroxide, sodium hydroxide, and ammonium hydroxide were all purchased from Sinopharm chemical reagent Co., Ltd. (China). Hydrazine hydrate and methyl 3-mercaptopropionate (MMP) were from J&K Scientific Ltd. (China). DAPI (C1002), 1 × PBS (C0221), MTT cell proliferation and cytotoxicity assay kit (C0009), and 0.25% trypsin-EDTA solution, BCECF-AM (2′,7′-bis(2-carboxyethyl)-5(6)-carboxyfluorescein acetoxymethyl ester) and were from Beyotime® Biotechnology (China). Sulfo-cyanine 5 NHS ester (Cy5-NHS) was obtained from Little-PA Sciences Co., Ltd. (China). TAT–SH (CGGGYGRKKRRQRRR), which composed of the protein transduction domain of $TAT_{47–58}$, a triple G spacer, and an N-terminal cysteine for binding with nanoparticles, was obtained from Shanghai Leon Chemical Ltd. (China).

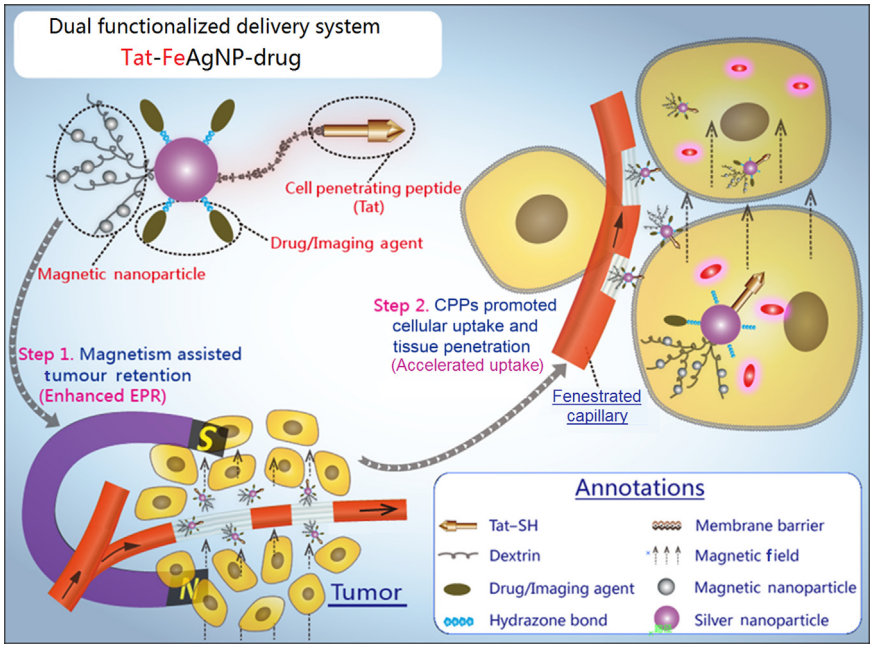

Figure 1 Illustrations of the dual functionalized Tat-FeAgNPs. Core of the system involved silver nanoparticles (AgNPs), which were surface-modified by Tat and iron oxide nanoparticles. As carriers, silver nanoparticles could load thiolated drugs *via* thiol-silver bondage. Generally, Tat-FeAgNPs delivered the loaded cargos by 1) magnetism-assisted tumor retention from circulation, and then 2) Tat helped the nano-vehicles penetrate the tumor barrier inside where it released the chemical bombs to fight the neoplastic cells.

2.2. *Preparation of metallic nanoparticles*

Silver nanoparticles (dex-AgNPs) were prepared by gentle reduction of silver ammonia using dextrin as both reducing and stabilizing reagent. In details, 5 mg (0.125 mmol) sodium hydroxide was added to 200 mL silver nitrate solution (1 mmol/L) under agitation, which yielded a yellow turbid solution. Then 1–2 mL ammonium hydroxide was added in droplet until the suspension become colourless and clear, indicating silver irons were complexed with ammonia. After that, 1.8 g dextrin was added to the silver ammonia solution, then the mixture was heated to 90 °C and maintained for 8–10 h till an isabelline solution (colour of silver nanoparticles) was formed, which displayed a characteristic surface plasmon resonance absorption at about 420 nm.

In order to prepare Ag-Fe_3O_4NPs (FeAgNPs), 3 mL more ammonium hydroxide were added into the afore-prepared AgNPs. The flask was then sealed and blown with nitrogen flows for 30 min to remove free oxygen, then 0.72 mmol iron salts (Fe^{3+}: Fe^{2+} = 2:1) dissolved in water were added dropwise and immobilized by the coating dextrin of AgNPs, producing FeAgNPs. Meanwhile, Ag-free dextrin was used to prepare Fe_3O_4NPs as control. All the products were precipitated and washed with 5-fold excess ethanol for three times to remove excess ammonium, and the sediments were re-dispersed with equivalent volume of double distilled H_2O (ddH_2O) for further usage.

As for TAT functionalization, 1 mL re-dispersed AgNPs (about 5 mg) or equivalent FeAgNPs was mixed with 10 μL TAT-SH (1 mg/mL) and be incubated at room temperature for 2 h, which produced Tat-AgNPs and Tat-FeAgNPs, respectively.

2.3. *Nanoparticle characterization*

Morphologies and chemical compositions of AgNPs, Fe_3O_4NPs, and FeAgNPs were analyzed by high-resolution transmission electron microscopy (HR-TEM, Fei Tecnai G2 F20) equipped with X-ray energy scanning and analysing apparatus. X-ray diffraction patterns of the nanoparticles with 2θ scanning range of 20°–90° were obtained by D/MAX 2500 X-ray diffractometer radiated using Cu/Kα (1.54) rays. Magnetic hysteresis loops of the three kinds nanoparticles were analysed by a superconducting quantum interference magnetometer.

2.4. *Synthesis of thiolated drugs*

Thiolated doxorubicin was synthesized by reacting doxorubicin (Dox, 1–5 mg/mL) with moderate excess (1:1.5) mercaptopropanohydrazide (MPH) in water without adjusting the pH, the reaction was carried out at dark conditions and proceeded for 24 h to make sure the transition was complete. To prepare mercaptopropanohydrazide, 11 mL methyl 3-mercaptopropionate and 12 mL hydrazine hydrate (50%, *v*/*v*) were reacted under nitrogen protection for 18 h, then the mixture were frozen-dried to remove water and excess hydrazine. Likewise, thiolated Cy5 was prepared by reacting Cy5–NHS (1 mg in 0.5 mL DMSO) with 5-molar excess cystine at room temperature. Unreacted Cy5–NHS and Dox could be removed by dialysis or precipitation after binding reactions with silver nanoparticles. The dialysis method is employed to calculate the drug loading efficiency and release behavior while the precipitation method was applied to prepare samples for all cell/animal tests since precipitation process provided a way of concentrating the drug-loaded nanoparticles which was important for animal test.

2.5. *HPLC analysis*

Hydrazine, methyl 3-mercaptopropionate, Dox, and their reaction products of mercaptopropanohydrazide, and thiolated Dox, were analysed by an Agilent 1260 high performance liquid chromatography

system equipped with a Luna® 5 μm C18 column (Phenomenex, 100 Å, 250 mm × 4.6 mm). The analytical parameters were set as: detection wavelength: 230 nm; injection volume: 10 μL; column temperature: 30 °C; mobile phase: 1 mL/min, acetonitrile:sodium heptanesulfonate solution (10 mmol/L, pH 3.0) = 35:65; elution time: 20 min.

2.6. Drug loading and release assay

Drug loading was simply performed by mixing and incubating silver nanoparticles with a given amount of thiolated drugs/dyes for 1–2 h. Unloaded drugs could be extracted from nano-vehicles using excess ethanol as described above. The sediment drug-loading nanoparticles were then re-dispersed with predetermined amounts of PBS for *in vitro* and *in vivo* experiments. Silver nanoparticle induced surface resonance energy transfer (SET)[16] was utilized for assessing the drug loading and release behaviours. In details, fluorescent spectrum of Dox, Dox–SH, FeAgNPs, mixtures of FeAgNPs with Dox and Dox–SH, respectively, (all dissolved in ddH_2O) were recorded and analyzed by an F4600 fluorospectrophotometer (Hitachi, Japan).

Nanoparticle-mediated cellular uptake and intracellular distribution of Dox was assessed by fluorescence microscopic analysis. Cells cultured in 35 mm glass-bottomed petri dishes (801001, Nest Biotechnology Co., Ltd.) were pre-treated with or without chloroquine (20 μmol/L) for 1 h. Later, Dox-loading AgNPs (AgNP-Dox), or mixtures of AgNPs with equivalent amount of free Dox (5 μmol/L) was added and incubated for 2 h, then the culture medium were replaced by fresh medium containing 1 μmol/L BCECF-AM and further cultured for another 1 h. Finally, cells were washed with 1 × PBS for three times, and be left with 200 μL buffer for CLSM (confocal laser scanning microscopy) imaging (Olympus Fluoview FV1000, Japan).

2.7. Cellular uptake and cytotoxicity assay

Cellular uptake assay was performed in 24-well plates, where MCF-7 cells were treated with equivalent Dox, AgNP-Dox, Tat-AgNP-Dox, FeAgNP-Dox, and Tat-FeAgNP-Dox (equivalent in Dox of 5 μmol/L for 4 h. In order to assess the influences of magnetic field on cellular uptake efficiency of nanoparticles, the culture plates were subjected to either an upward or downward magnetic field produced by an external magnet (0.3 T, 8 × 12 cm) for 4 h. Then cells were fixed, and the nuclei stained by DAPI, and finally subjected to fluorescence imaging analysis (Leica, DMI300B).

Cytotoxicity was assessed by MTT assay. Generally, MCF-7 cells were seeded in 96-well plates and be incubated with a serial concentrations of Dox, AgNP-Dox, Tat-AgNP-Dox, FeAgNP-Dox, and Tat-FeAgNP-Dox, respectively (dispersed in cell medium containing 10% FBS). As above mentioned, plates containing FeAgNP-Dox and Tat-AgNP-Dox were assigned to receive 4 h-exposure of external magnetic field. Then all the plates were replaced with fresh medium and were further incubated for 24 h in advance of MTT assay. IC_{50} values of different drugs were calculated by the Graphpad prism 5.0 software.

2.8. In vivo tumor targeted drug delivery and anti-tumor assessment

Tumor drug delivery was assessed on a subcutaneous xenograft mouse model. The tumor-bearing mice were produced by subcutaneously injecting MCF-7 cells (1×10^6 cells in 150 μL serum-free medium) at the right axillary site. When tumor grew to the size of 400–500 mm^3, mice were randomly assigned to six groups ($n = 3$), which received a single dose i.v. injection of free Cy5, or Cy5-labelled AgNPs, Tat-AgNPs, FeAgNPs, Tat-FeAgNPs, respectively (equivalent with Cy5 at the dose of 20 nmol/kg). As for mice given FeAgNP-Cy5 and Tat-FeAgNP-Cy5, a magnet (0.3 T, 10 mm × 10 mm) was laid close to the tumor to produce an external magnetic field. The whole body fluorescent signals at 1, 4, 12, and 24 h, were recorded by the IVIS spectrum imaging system (Perkin-Elmer). Mice receiving the final imaging at 24 h were immediately anesthetized and be performed with heart perfusion. Then the tumors were excised, weighted and divided into two parts: one part of the tumor was processed by fixation, dehydration, and cryostat section for microscopic imaging; while the other part of tumor was further divided for quantitative analysis, with part of it being homogenized and extracted using alcohol for fluorescence analysis; the left part of tumor being digested by 2 mL HNO_3–H_2O_2 mixture (1:1), which was then subjected to inductively coupled plasma-mass spectrometry (ICP-MS, Agilent 7700X) for determination of silver concentration.

Anti-tumor efficacy of Dox-loaded nanoparticles was assessed on a parallel batch of tumor-bearing mice. Animals were randomly assigned into five groups ($n = 6$) and began with regimentation of Dox-loaded nanoparticles (equal to 1.5 mg/kg of free dox) when tumor reached 200 mm^3. Tumor volume (V) was calculated based on Eq. (1):

$$V = 0.5 \times L \times W^2. \quad (1)$$

where L is tumor length and W is tumor width. To compare the tumor inhibition effects of different drugs, a clinically applied therapeutic parameter, specific growth rate (SGR) of tumor, was utilized to exclude the within-subject variations. Generally, SGR was calculated based on Eq. (2):

$$\mathrm{SGR} = \mathrm{Log}\left(V_t/V_0\right)/(T_t - T_0) \quad (2)$$

where V_0 and V_t, referred to the measured tumor volume at time T_0, and T_t, respectively[17–19]. Tumor volume was recorded every other day along with the routine administration. With no further declaration, all animal studies were performed under the guidance of Institutional Animal Care and Use Committee (IACUC) of Shanghai Institute of Materia Medica, Chinese Academy of Sciences (Shanghai, China). Mice would be humanely sacrificed if either body loss exceeded 20%, or tumor volume reached above 2000 mm^3.

2.9. Statistical analysis

Intergroup differences of both *in vitro* and *in vivo* data were analysed by one-way or two-way ANOVA test based on Fisher's LSD test, which were carried out on a Graphpad prism software (Version 5.0). $P < 0.05$ was defined as statistically significant during multiple comparisons between different groups of data.

3. Results and discussion

3.1. Characterization of FeAgNPs

In recent years, synthesis of iron alloy nanoparticles with silver had attracted extensive interests from different disciplines[20,21]. As drug vehicles, the alloy nanoparticles not only possessed magnetism from

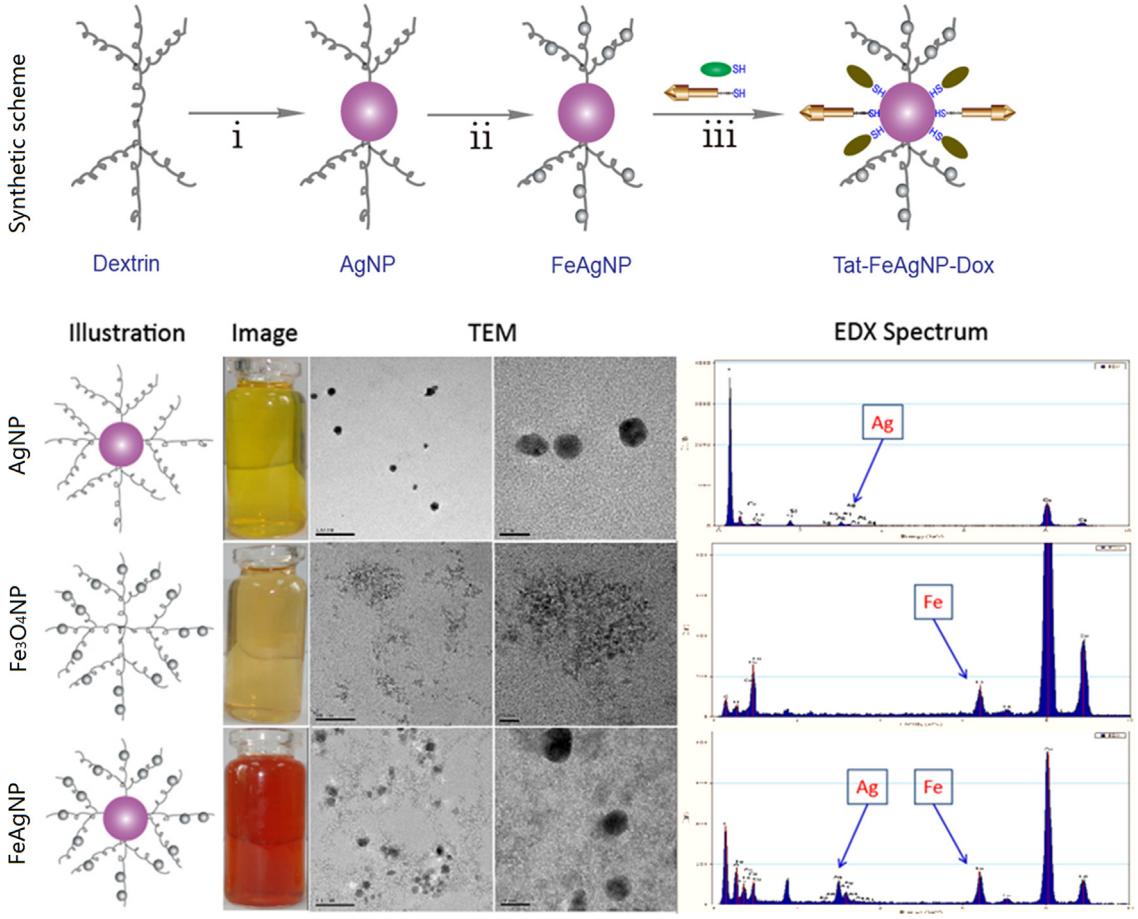

Figure 2 Synthetic scheme of preparing Ag-Fe_3O_4 nanocomposites (Up), TEM-EDX characterizations of as-prepared metallic nanoparticles (Down), from top to the bottom were silver nanoparticles (AgNPs), iron oxide nanoparticles (Fe_3O_4NPs), and Ag-Fe_3O_4 nanocomposites (FeAgNPs), respectively. Reaction conditions: i) Dextrin, 1.8 g; H_2O, 200 mL; [Ag^+], 1 mmol/L, [NH_3], 2.5 mmol/L, 90 °C, 4 h; ii) 3 mL ammonium hydroxide (25%); [Fe^{3+}], 0.48 mmol; [Fe^{2+}], 0.24 mmol; nitrogen flow, 80 °C, 30 min; iii) FeAgNPs, 50 mg; Dox, 25–250 μg; Tat–SH, 10 μg; H_2O, 1 mL; Room temperature, 2 h.

ferroferric oxide, but also acquired features of silver nanoparticles such as optical and thiol binding ability. However, since those physiochemical properties were dependent on the intrinsic crystal structures of atom packing[22], formation of alloy particles might result in function loss for both particles. In comparison, crosslinking the two together could retain the crystal structures and their related physiochemical features for both nanoparticles, yet the chemistry for straightforward crosslinking was challenging because the weak affinity of Fe_3O_4NPs towards various functional groups (hydroxyl, carboxyl, etc.) could not yield a stable linkage[23], leading to unfavorable agglomeration. Alternatively, both silver and Fe_3O_4NPs belonged to inorganic nanoparticles, which shared a common *in situ* formation pathway of preparing stable nanoparticle dispersions[24,25], suggesting the two could be assembled together by sequentially capping the finely formed nanoparticles in the same polymeric framework. To this regard, dextrin was chosen in our system as the stabilizing agent because 1) the primary hydroxyl groups from glucose units of dextrin could serve as both reducing and binding sites for silver nanoparticles[26], and 2) dextrin and its derivatives were the most frequently utilized stabilizers for preparing aqueous clinical brand of iron oxide products[27]. Accordingly, we proposed a two-step procedure for the synthesis of well dispersed aqueous Ag-Fe_3O_4 nanocomposites (Fig. 2). The as-prepared nano-vehicles were well dispersed in water, yet insoluble in ethanol because of the coating dextrin, thus could be precipitated and re-dispersed by solvent exchange from alcohol to water (Supplementary Information Fig. S1), which was more convenient than the routinely centrifugal method during purification and concentration process. Morphologies and chemical compositions of the prepared FeAgNPs were shown in Fig. 2. By comparing the TEM and EDX spectra with AgNPs (up) and Fe_3O_4NPs (middle), it was apparently to identify that the 15 nm sized AgNPs were surrounded by ultra-small Fe_3O_4NPs (1–2 nm). XRD spectrums (Fig. 3A) further approved that the as-obtained Ag-Fe_3O_4 were composed of identical crystalline particles which corresponded to JCPDS cards of silver (04–0783) and magnetite (16–0629), respectively. Of note, although crystalline structure of the Fe_3O_4 was not affected in the nanocomposite, the Ag-Fe_3O_4 showed decreased saturation magnetization (3.8 emu/g) as compared with as compared with silver-free Fe_3O_4-NPs (9.0 emu/g). To further test whether the separately formed silver and iron oxide particles were interlinked, the water dispersion of the nanocomposites was lied nearby a magnet, results showed that all the particles could be driven by the externally applied magnetic field (Fig. 3C), suggesting that silver nanoparticles were crosslinked with magnetic nanoparticles. As for drug delivery, the AgNPs would serve as a "sled" and carry thiolated drugs *via* the silver-thiol bond, whereas the surrounding Fe_3O_4NPs would serve as

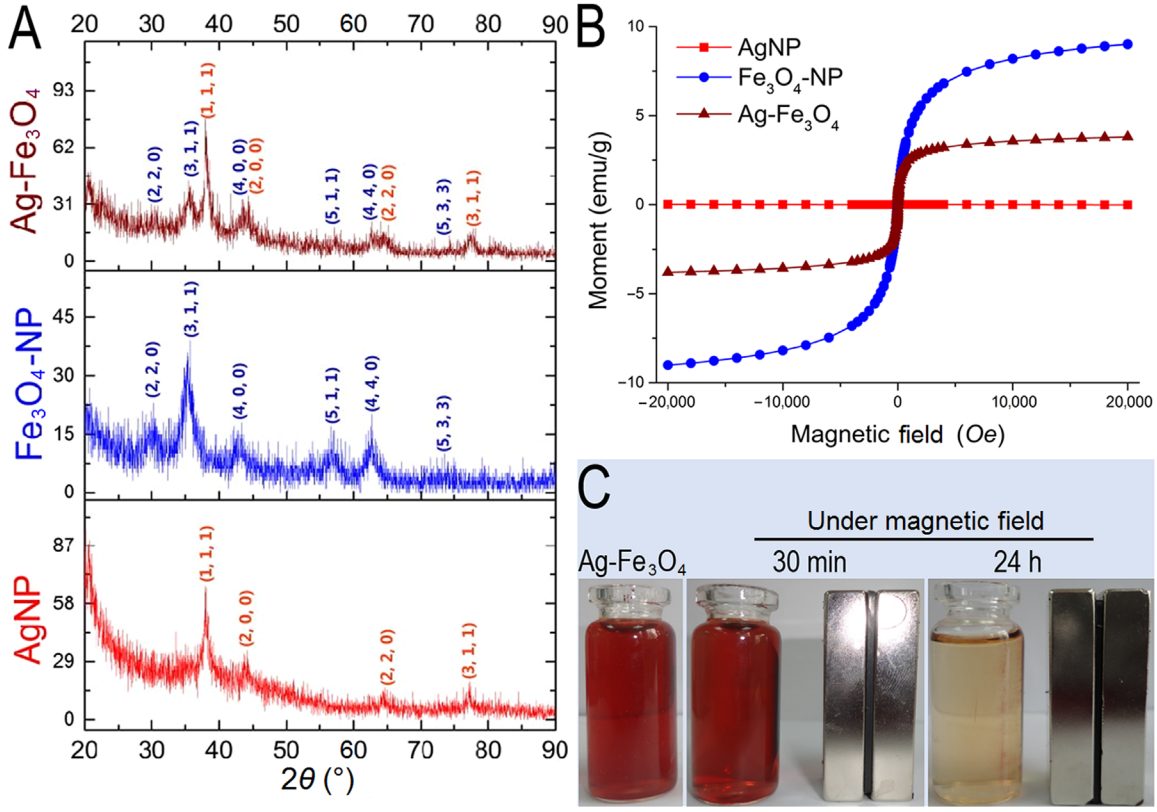

Figure 3 XRD (A) and hysteresis loops (B) of the prepared metallic nanoparticles; (C) magnetic responsiveness of Ag-Fe_3O_4 to an aside placed magnet.

"dogs" driving the sledge to a specific organ under the guidance of the external magnetic field.

3.2. *Drug loading and release*

The FeAgNPs thus prepared were ready to carry thiolated drugs for further applications. In order to prepare thiolated doxorubicin, we synthesized a small –SH containing linker (3-mercaptopropanohydrazide) for reacting with doxorubicin (Fig. 4A). As illustrated, 3-mercaptopropanohydrazide would form a hydrazone bond with the C-13 ketone from doxorubicin, yielding a thoilated drug with degradable bonds[28–30]. The reactants of hydrazine, methyl 3-mercaptopropionate, their intermediate hydrazide product, Dox, as well as the final thiolated product were stepwise analysed by a HPLC method (Fig. 4B). Results showed that the two-step reaction was proceeding as designed with high yields. Interestingly, by aligning the spectrum of the final product with that from the reacting Dox and mercaptopropanohydrazide (MPH), two identical peaks appeared in the HPLC spectrum, which could be ascribed to Dox–SH and its oxidized form of disulfide dimer. The binding patterns of both Dox–SH and its dimer rely on the sulfur atoms, and the main difference between the two lies in the binding strength with metal surface. Although binding strength of the dimer counterpart is weaker, the weakly bonded disulfide chemicals, the disulfide bonds were also capable of binding to silver nanoparticles[31] and sometimes would break into more stably bonded monothiolate. Therefore, the as-obtained thiolated drugs could be used directly without further purification.

Similar to Förster resonance energy transfer (FRET) that occurred between two molecular dipoles (usually defined as donor and receptor, respectively), dipole-surface energy transfer (SET) occurred between fluorescent molecule and metallic nanoparticles often led to photo-quenching effect[16,32]. Importantly, the quenching efficiency was sensitive to changes of fluorophore-surface distance, as Förster distances for efficient fluorescence quenching was reported to be less than 10 nm[13]. Therefore, it was possible for us to discern surface conjugated Dox-SH with free Dox from fluorescent spectra. As shown in Fig. 4C, thiolation did not affect the fluorescence of doxorubicin, because the fluorescent profiles of Dox and Dox–SH almost overlapped each other. Interestingly, once Dox and Dox–SH were separately mixed with equivalent AgNPs, the peak fluorescence of thiolated Dox decreased dramatically to only 7.0% of the original intensity, whereas the mixture of Dox and AgNPs retained 82.9% of the initial fluorescence. The complete quenching of mixture of Dox–SH and AgNPs indicated that a stable bond between the two compounds was formed, in comparison with mixtures of Dox and AgNPs.

Drug entrapment efficiency (EE) and drug loading efficiency (LE) was assessed using dextrin immobilized AgNPs. Since the drugs was uploaded on the nano-carriers *via* the thiol–Ag bondage, loading efficiency was calculated based on the total weight of dextrin-AgNPs and the weight of silver, respectively (Supplementary Information Fig. S2A). Results showed that drug encapsulation efficiency was dependent on the feeding concentration of Dox–SH. For example, the calculated EE was about 90% when feeding Dox–SH less than 150 μg/mL was applied, further increasing drug concentration led to a drastically reduction of EE to 58.9% when the feeding concentration of Dox–SH reached

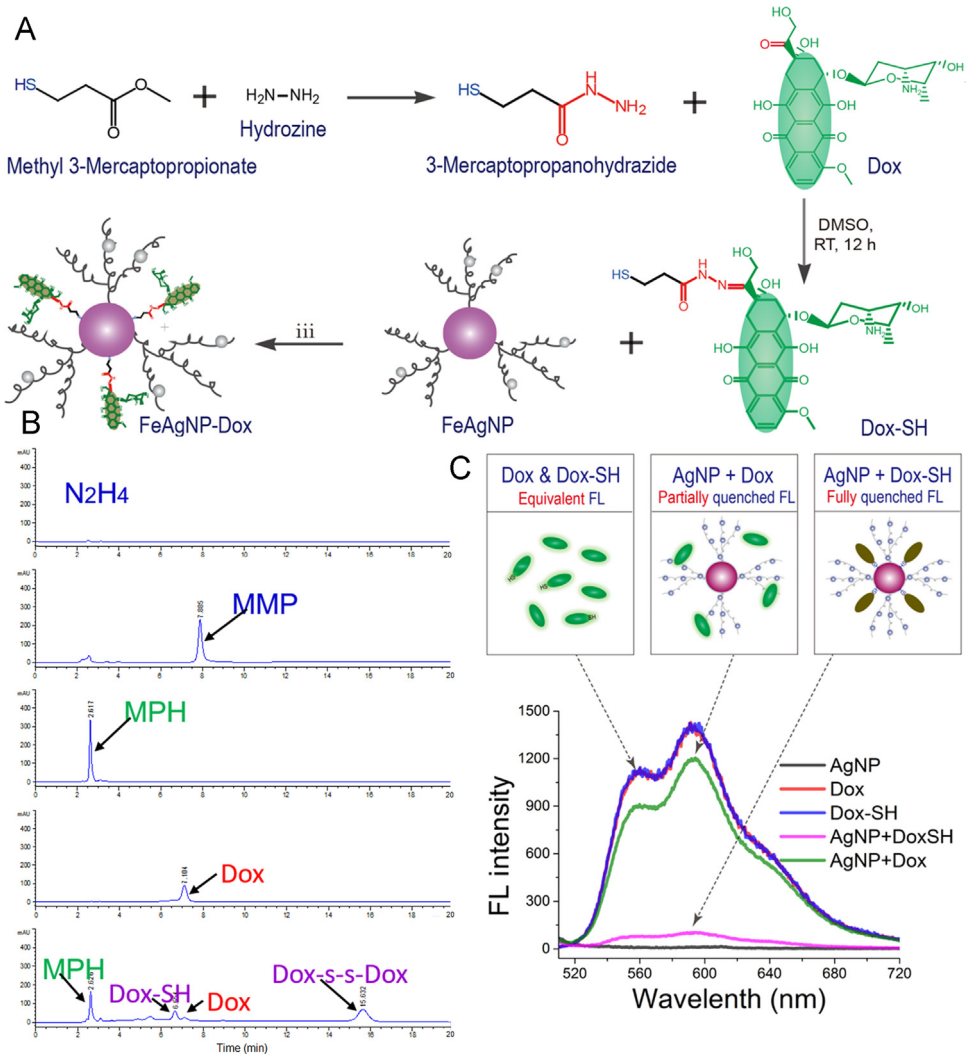

Figure 4 (A) Schematic illustrations of preparing Dox–SH and Dox-loaded FeAgNPs; (B) HPLC spectrums of the reactants and products. From top to bottom are hydrazine, methyl 3-mercaptopropionate (MMP), and synthesized mercaptopropanohydrazide (MPH, intermediate product) from reaction step (i). Dox, doxorubicin; Dox–SH, final product. (C) Fluorescent spectra of Dox, Dox–SH, and as-prepared FeAgNP-Dox dissolved in ddH_2O (λ_{EX} = 495 nm, λ_{EM}, 510–720 nm, PMT voltage at 400, and split width = 5 nm).

250 μg/mL. Accordingly, the maximal loading efficiency of Dox–SH was calculated to be around 0.3% by the total weight of dextrin-AgNPs, and around 8% by the silver weight. After loading onto the silver vehicles, doxorubicin could be released *via* the pH sensitive hydrazone bond. To test the pH sensitivity of this system, we monitored the *in vitro* release behaviour of Dox-loaded nanoparticle (AgNP-Dox). Our results demonstrated that free Dox could be released in a pH-dependent pattern, and the cumulative released drug under different pH within 2 h was about 20.5% (pH 7.4), 38.1% (pH 6.0), and 47.1% (pH 5.0), respectively (Supplementary Information Fig. S2B), providing a solid support to the claim that our systems would release the loaded drug in a pH-dependent pattern. However, it was worth noting that an unexpected high release of drugs from AgNP-Dox was found at pH 7.4, which was supposed to be stable at neutral conditions as reported that Dox-loading gold nanorods *via* hydrazone– and Au–S bonds manifested minimal release of Dox at pH 7.4[33]. With this respect, the enhanced release of Dox at pH 7.4 from our system might partially be ascribed to the dissolution of the weaker Ag–S bond[34].

Linker-mediated Dox loading and release could be further identified by CLSM assay. As shown in Fig. 5, simply mixing Dox with silver nanoparticle did not affect the endocytic process of the drug, which preferentially accumulated inside the nucleus. As compared, Dox carried by AgNPs *via* the liker was found to be enriched at perinuclear regions. Moreover, by mapping the intracellular pH of MCF-7 cells with BCECF (green fluorescence with stronger signals at higher pH), it was apparently to see the Dox's signal (red fluorescence) was more intensive at low pH regions. And chloroquine treatment (sparing the pH induced fluorescence variation) did not affect the distribution patterns of nano-particulate Dox, suggesting the loaded drugs had not been sufficiently released during the 2 h's treatment, which otherwise would result in significant red signals in the nucleus. Notably, the preferential distribution of AgNP-Dox at low pH region (probably the endosome) herein would facilitate the intracellular release of the hydrazone bonded Dox, which had been approved by the *in vitro* release tests (Supplementary Information Fig. S2B).

3.3. *Cellular uptake and cytotoxicity assay*

As mentioned above, the principle of the Tat-FeAgNP was based on 1) magnetism-assisted nano-vehicle retention (caused by EPR mediated tumor passive targeting), and 2) Tat-mediated blood tumor barrier penetration and tumor cellular uptake. To evaluate the influences of magnetism and Tat modifications *in vitro*, MCF-7 cells were treated with various regimens of the test compounds under different directions of the magnetic force. As shown by the cellular uptake of fluorescent markers in Fig. 6A, it was apparent to see that 1) Tat modification significantly promoted cellular uptake of the nano-vehicles (Tat-AgNP-Dox *vs* AgNP-Dox; Tat-FeAgNP-Dox *vs* FeAgNP-Dox); 2) Crosslinking with Fe_3O_4NPs led to a reduced cellular uptake when comparing with their iron-free counterparts (AgNP-Dox *vs* FeAgNP-Dox; Tat-AgNP-Dox *vs* Tat-FeAgNP-Dox); 3) magnetism could help to enhance cellular

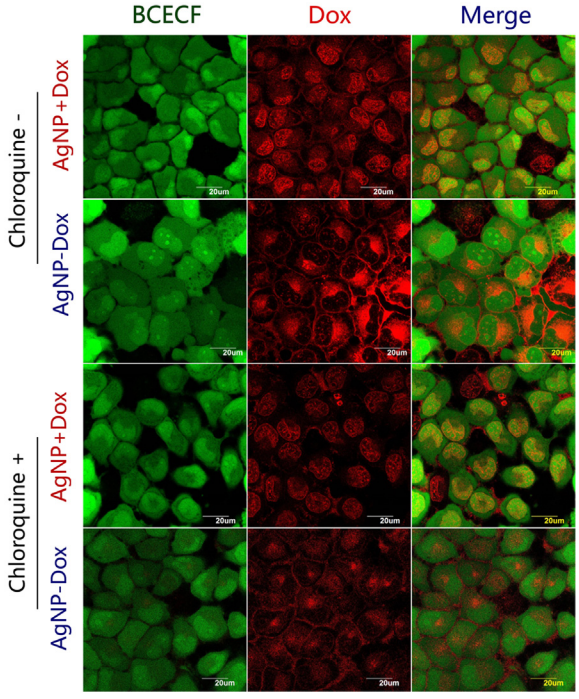

Figure 5 pH-dependent intracellular distribution of Dox in MCF-7 cells fed with AgNP–drug conjugate *via* designed mercaptopropanohydrazide. Physical mixture of AgNP with Dox was used as non-conjugate control. Cytosolic pH of MCF-7 cells were mapped by a pH probe (BCECF-AM), which showed enhanced green fluorescence in response to decreased the environmental pH.

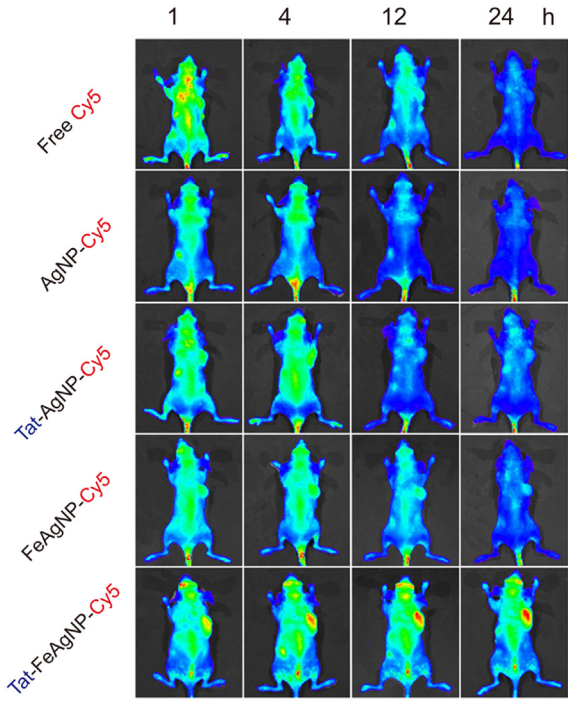

Figure 7 Optical images of tumor bearing mice at different time post administration of Cy5 and Cy5-loaded nano-vehicles.

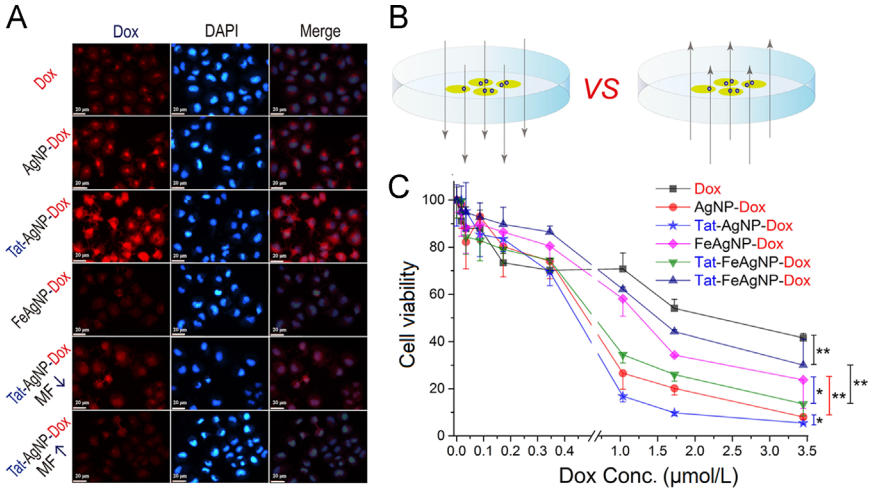

Figure 6 Cellular uptake (A) and cell inhibition assay (C) of Dox and Dox-loaded nanoparticles. Test samples include Dox (doxorubicin), AgNP-Dox (Dox-loaded silver nanoparticles), Tat-AgNP-Dox (Tat modified, Dox-loaded silver nanoparticles), FeAgNP-Dox (Dox-loaded silver-iron oxide nanocomposites), Tat-FeAgNP-Dox (Tat modified, Dox-loaded silver-iron oxide nanocomposites). As for cells treated with FeAgNP-Dox and Tat-FeAgNP-Dox, an 8 cm × 12 cm magnet (0.3 T) was applied upon or below the plates to producing a externally upward or downward magnetic field (MF) to the cultured cells, as illustrated in (B). $^{*}P < 0.05$; $^{**}P < 0.01$.

uptake of the magnetized nanoparticles (Tat-FeAgNP-Dox with up or downward magnetic field). While Tat functionalization promoted cell penetrating of the nano-devices was expected, crosslinking with Fe_3O_4NPs obviously decreased the cellular uptake of the attached silver vehicles due to increased hydrodynamic size of the final composites. Our cell culture results also demonstrated that magnetism could play the role of either an enhancer or an attenuator, depending on whether the directions of the applied magnetic field was set towards the cultured cells (as portrayed in Fig. 6B). Interestingly, although silver and iron oxide nanoparticles both showed a degree of cell inhibiting potential (23% for AgNP, and 17% for Fe_3O_4-NP, Supplementary Information Fig. S3), they otherwise displayed opposite effect on cell viability when incorporated in the dual nano-systems. Whilst being an anti-tumor agent itself, silver nanoparticles could synergistically inhibit cell proliferation with the loaded drugs thereby producing enhanced cytotoxicity (AgNP-Dox > Dox), loading of Fe_3O_4NPs nevertheless resulted in reduced inhibition on cell growth (AgNP-Dox > FeAgNP-Dox; Tat-AgNP-Dox > Tat-FeAgNP-Dox), which apparently could be attributed to the increased hydrodynamic size of the systems as previously discussed. Consequently, MTT tests gave IC_{50} of Dox-loaded nanoparticles in the following order (Fig. 6C): Dox (1.82 μmol/L) > Tat-FeAgNP-Dox with upward MF (1.55 μmol/L) > FeAgNP-Dox with downward MF (1.14 μmol/L) > Tat-FeAgNP-Dox with downward MF (0.63 μmol/L) > AgNP-Dox (0.57 μmol/L) > Tat-AgNP-Dox (0.46 μmol/L).

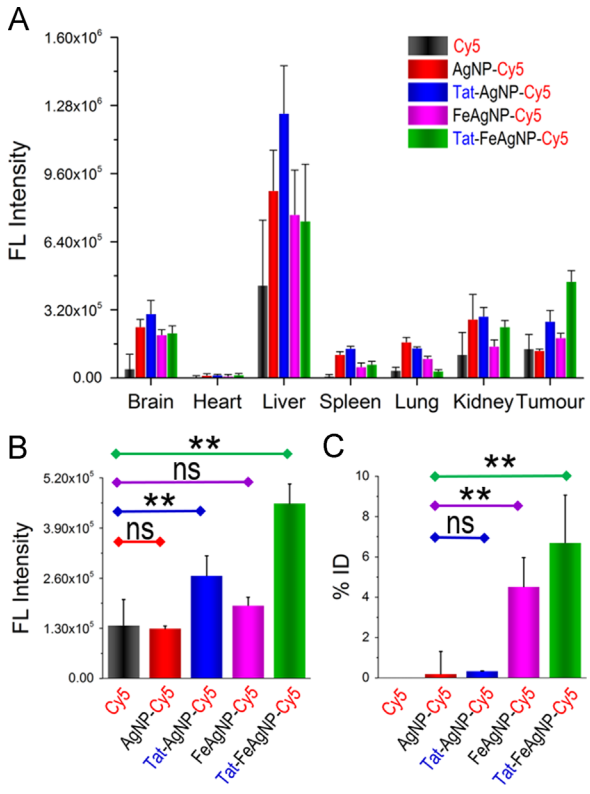

Figure 8 (A) Quantitative fluorescence of tissue homogenates of mouse 24 h post administration. (B) and (C) represented tumor content of drugs (Cy5, B) and nanoparticles (silver, C), respectively. $^{*}P < 0.05$; $^{**}P < 0.01$.

3.4. *In vivo delivery efficiency and anti-tumor assessment*

In vivo delivery efficiency was assessed by using a near infrared dye, Cy5, to track the pharmacokinetic behaviours of the nano-carriers. Whole-body imaging and tissue homogenates analysis were carried out to depict the bio-distribution pattern, as well as the individual tissue loads of Cy5 for the testing nano-carriers. *In vivo* imaging results showed that Tat-FeAgNP-Cy5 was accumulated at the tumor most efficiently (Fig. 7), and this finding was further confirmed by optical images of the excised tumors (Supplementary Information Fig. S4). Of note, the *ex vivo* test showed that the fluorescence in excised tumor was even stronger than those in the liver and the spleen. However, the total quantity of the fluorescence in the individual organ calculated from tissue homogenates demonstrated that liver remained as the primary target for nanoparticle accumulation (Fig. 8A), a phenomenon that

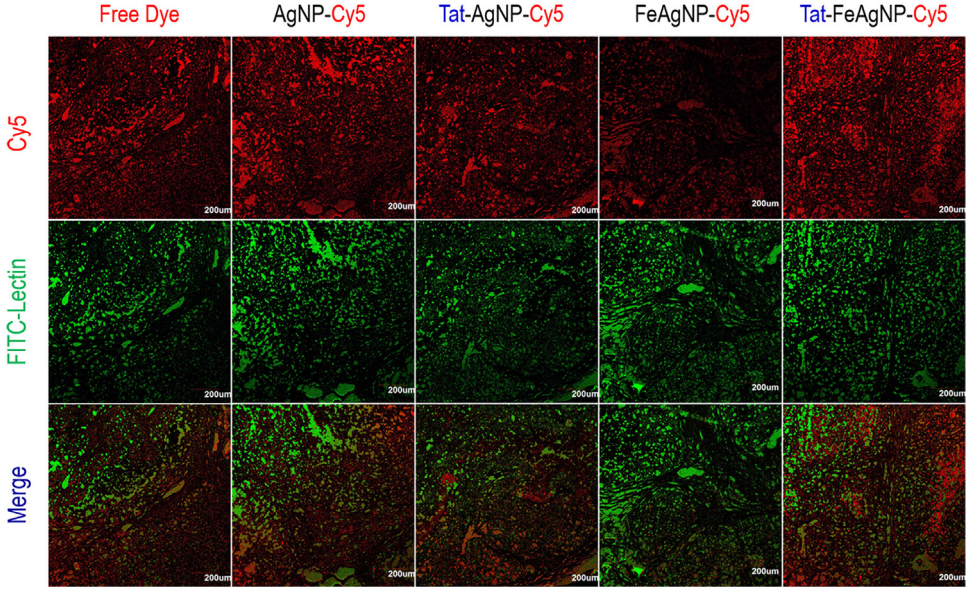

Figure 9 Tumor sections of mice treated with Cy5-labelled nanoparticles or free dyes (Red fluorescence). FITC-labelled lection was used to mark the tumor vasculatures (Green fluorescence).

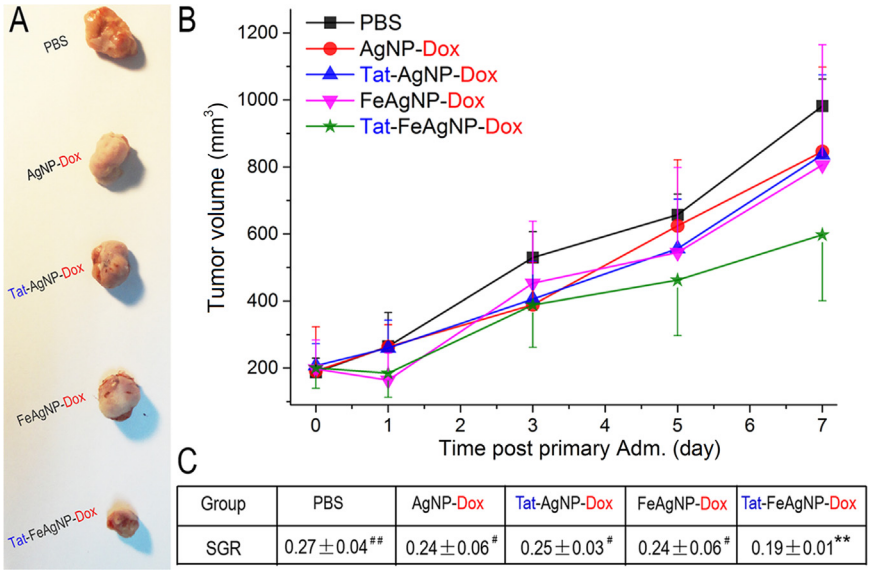

Group	PBS	AgNP-Dox	Tat-AgNP-Dox	FeAgNP-Dox	Tat-FeAgNP-Dox
SGR	$0.27\pm0.04^{\#\#}$	$0.24\pm0.06^{\#}$	$0.25\pm0.03^{\#}$	$0.24\pm0.06^{\#}$	$0.19\pm0.01^{**}$

Figure 10 Anti-tumor efficacy of Dox-loaded nanoparticles. (A) Tumors excised from mice at 7th day; (B) tumor growth profiles of mice treated with different drugs; (C) calculated specific growth rate (SGR) of mice tumors at the 7th day post initial administration. Note, significance level of inter-group comparisons between Tat-FeAgNP-Dox-treated mice with other group were marked as $P<0.05$), $P<0.01$; and test significance between mice receiving PBS with others were marked as $^{*}P<0.05$, $^{**}P<0.01$.

accounted for in terms of the dominant mass compared with tumor (1.66 ± 0.18 g *vs* 0.32 ± 0.15 g). By quantitatively analysing the homogenates data, it was revealed that the substantial tumor intake of the dual functional system relied on Tat and the external magnetism. First, as compared with free dye and unmodified AgNP-Cy5, Tat-AgNP-Cy5 dosed mice displayed stronger fluorescence signals in all of the organs examined (Fig. 8A), demonstrating that Tat would promote the uptake of the functionalized vehicles. Second, while FeAgNP-Cy5 was less favourably taken by the main organs when comparing with that of AgNP-Cy5, the iron-silver nanocomposites nevertheless gained enhanced tissue retention by the tumor when a localized magnetic field was applied (Fig. 8A and B). As with the *in vitro* test, the incorporation of iron oxide nanoparticles resulted in a reduction in cellular uptake efficiency as well as the cell inhibition functions of silver nanoparticles (Fig. 6). Hence the conversely increased tumor uptake could be ascribed to enhanced tumor retention from circulation promoted by external magnetism. Interestingly, microscopic results showed that the tumor accumulated FeAgNPs were mainly retained in the vasculatures (marked by FITC-lectin as green fluorescent regions) and manifested overlapped Cy5 signals (red fluorescence) with FITC-lectin. In comparison, free dye (Cy5) and other nanoparticles (AgNPs, Tat-AgNPs, and Tat-FeAgNPs) could extravasate from tumor vasculature and into the interstitial space, thus showing overflowed red fluorescence outside the tumor vessels (Fig. 9).

Two issues need to be noted in this *in vivo* study are as follows. Firstly, since the Cy5 is chemically bonded with cysteine *via* a stable amido bond, release of Cy5 from AgNP relies on the dissociation of amido bond which gives free Cy5, or degradation of Ag–S bond, or lysis of the nanoparticles, which gives the thiolated Cy5. On this account, the dissociation of Cy5 from the nanoparticles would be less pH-dependent, and thus more stable as compared with Dox–SH. Secondly, although conjugation of Cy5 with the AgNP will lead to photo-quenching effect of the fluorophore to some extent, the fluoresce of the loaded dye is not fully quenched (for example, the remnant FL of the binded Dox still accounts for 12% of its free form), and more importantly the remnant fluorescent signal would be detected by the *in vivo* imaging apparatus. As our results just compared the targeting efficiency of testing drugs to organs in the same body, differences of FL between different drugs were normalized and the objective comparisons between different groups were provide.

It was worth noting that, compared to tumor homogenates fluorescence data, the detected tumor content of AgNPs and FeAgNPs in the form of silver, was much attenuated. For example, the calculated inter-group ratio among different nanoparticles (AgNPs, Tat-AgNP, FeAgNP, Tat-FeAgNP) by fluorescence was 1:2.1:1.5:3.5; whereas by silver weight the inter-group ratio was calculated to be 1:1.8:23.8:35.3. This variation can be ascribed to the differences of analytical method, as well as the tissue penetration and release properties of the testing nanoparticles. In details, the tumor silver content was analysed by digesting the whole tumor with H_2O_2/HNO_3 solution, which gave the vehicle content irrespective of its microscopic distribution and drug release properties. In comparison, tumor Cy5 content was analysed using the tumor homogenates, which were treated with methanol to extract the free Cy5. Thereby unreleased Cy5 and proteins were precipitated along with the vehicles after adding methanol which was not to be determined. On this account, AgNP-Cy5, Tat-AgNP-Cy5 could penetrate into the tumor, be digested and release the loading Cy5, which can be detected by fluorospectrophotometry. In comparison, although FeAgNP-Cy5 could accumulate in the tumor more efficiently than AgNP-Cy5 and Tat-AgNP-Cy5 under the guidance of external magnetic field, it could not reach deep into the tumor, and most loaded Cy5 was not released. Therefore, although FeAgNP-Cy5 showed higher tumor retention (higher silver content) than Tat-AgNP-Cy5, its released Cy5 was fewer, therefore showing less "tumor Cy5 content". Overall, it was depicted that Tat-FeAgNP-Cy5 would display the most advanced tumor accumulation. And the tumor retained Tat-FeAgNPs analysed by ICP-MS was $6.7\pm2.4\%$ of the administrated dose

(Fig. 8B), which was significantly higher than most of the findings reported in the literature[8].

Real-time anti-tumor effects were assessed by repeated injections of the Dox-loaded nanoparticles every other day. Of note, the xenograft MCF-7 tumors displayed a fast growing profile, of which the size increased from 187.3 ± 41.8 to $981.4 \pm 80.7\ mm^3$ within one week after initiation of the treatment. As time went on, tumor growth of control decreased and a pleatu was reached at 9th day, which attenuated the therapeutic effects of the testing nanomedicine as the tumors of those mice were still growing (data not shown). Thereby, the volumetric data of tumors within the first week was optimum in assessing the efficacy of nanomedicine (Fig. 10A) without bigotry because all tumors of animals were still in the same growing stage. The volumetric profiles were shown in Fig. 10B, to exclude the with-group variations between different tumors, herein the specific growth rate (SGR) of each tumor was calculated (Fig. 10C) in order to monitor the tumor inhibition effects as it had been clinically applied as a powerful therapeutic index in the evaluation of treatment responses of heterogeneous human tumors[17–19]. In agreement with findings by using Cy5 dye as the model drug, tumor growth measurements demonstrated that Tat-FeAgNP-Dox yielded the most significant tumor-inhibitory effects among all the testing nanomedicines, which manifested a reduction of 29.6% on the SGR of tumor one week after initial treatment comparing with the PBS group ($P = 0.009$; calculated SGR as 0.27 ± 0.04, and 0.19 ± 0.01 for mice treated with PBS and Tat-FeAgNP-Dox, respectively). In contrast, the SGR reduction (with comparison to PBS control) of AgNP-Dox, Tat-AgNP-Dox, and FeAgNP-Dox were 11.1%, 7.4%, and 11.1%, respectively, and none of them showed significant differences ($P > 0.05$). Furthermore, the SGR value of Tat-FeAgNP-Dox was significantly lower than those from all the other three groups, including AgNP-Dox, Tat-AgNP-Dox, and FeAgNP-Dox ($P < 0.05$). Taken together, these results convincingly showed that the Tat-FeAgNP-Dox was superior to other NPs at targeting the tumor site.

The successful applications of Tat-FeAgNPs in delivering doxorubicin and Cy5 to the xenograft tumors of mouse supported our hypothesis that augmented EPR effect together with enhanced tissue/cell penetration would facilitate a substantially improved cancer drug delivery. Our results, on the other hand, reconfirmed the dilemma for the conventional nano-vehicle-based drug delivery system. As known, human tumor and all the other organs were interconnected by the circulation system, where the designed nanocarriers of varied forms were delivered *via* blood into all the organs/tissues indiscriminately. On this account, drugs and nanoparticles were delivered to the tumor in almost a random pattern[7]. Therefore, more efforts should be focused on designing materials that could change the *in vivo* biodistribution and gain fast access to the tumor site. Herein, our dual functional system, though might not strictly be categorised as "active targeting", yet achieved increased tumor loads compared with nanoparticles which relied on EPR effect. Furthermore, since the targeting process of this system relied on external magnetism, it was reasonable to assume that the Tat-FeAgNPs were apt to deliver loaded drugs/imaging reagents to any organs of the body where localized magnetic field was applied. To test this hypothesis, we had carried out another test by attaching a magnet to the heads of mice, finding that intravenously injected Tat-FeAgNP-Cy5 can more efficiently accumulate at the brain than either single-functionalized nanoparticles (Tat-AgNP-Cy5, FeAgNP-Cy5), or free Cy5 control (Supplementary Information Fig. S5). The new results again supported our hypothesis that external magnetism along with CPPs can synergistically work together to improve the delivery efficiency of nanocarriers. As the available nanomaterials were all designed for certain targets, they might be incompetent as drug carriers for other specific targets. Therefore Tat-FeAgNPs might serve as the first multi-target delivery systems in the future.

4. Conclusions

In this paper, we re-evaluated the targeting dilemma for conventional nano-vehicles in cancer drug delivery and were convinced that the primary reasons could be attributed to the limited EPR effect and tumor barriers. Based on this, we proposed a dual functional system that afforded improving tumor retention and promoting tumor uptake at the same time. The system was based on dextrin-coated silver nanoparticles, which were then crosslinked with iron oxide nanoparticles and cell penetrating peptide (Tat), producing the dual functional Tat-FeAgNPs with both superparamagnetic property as well as cell penetrating ability.

The microscopic structure of silver-iron oxide nanocomposites was analysed by TEM and EDX assay, which demonstrated that silver nanoparticles of about 15 nm were surrounded by ultra-small iron oxide nanoparticles. In order for loading drugs, we designed and synthesized an –SH containing linker, 3-mercaptopropanohydrazide. The small linker contained both a thiol and a hydrazide group, which enabled it to be loaded onto the nanoparticles *via* thiol-silver bondage. In addition, 3-mercaptopropanohydrazide linker could form a pH sensitive bond with the carbonyl group on drugs such as doxorubicin. Results from the drug loading and release studies indicated that thiolated Dox could attach onto the surface of silver nanoparticles, resulting in an efficient fluorescence quenching of up to 93%. Furthermore, the release of loading Dox was pH dependent, as the cumulative release of Dox after 2 h incubation at pH 5.0 was 2.3-fold over that at pH 7.4. The intracellular release of FeAgNP-Dox in MCF-7 cells also demonstrated that the nano-vehicles could release the encapsulated drugs in a pH dependent mode.

In vitro cellular uptake and cell inhibition studies were carried out to assess the benefits of the incorporating Tat and iron oxide nanoparticles to the silver nanoparticles. The results demonstrated that Tat significantly promoted cell uptake and cytotoxic effect of the nanoparticles. Whereas post-immobilization of iron oxide nanoparticles would result in increased hydrodynamic size, thereby causing a decreased cellular uptake and cytotoxicity; external magnetism could promote cell uptake with decreased IC_{50}, upward magnetic field produced reversed effect. Generally, MTT tests gave IC_{50} of Dox-loaded nanoparticles in the following order: Dox (1.82 μmol/L) > Tat-FeAgNP-Dox with upward MF (1.55 μmol/L) > FeAgNP-Dox with down MF (1.14 μmol/L) > Tat-FeAgNP-Dox with downward MF (0.63 μmol/L) > AgNP-Dox (0.57 μmol/L) > Tat-AgNP-Dox (0.46 μmol/L).

The feasibility of the dual functional system was further assessed in MCF-7 xenograft tumor mouse model. It was depicted by the whole body imaging as well as quantitative homogenates analysis, that Tat and iron oxide nanoparticles, both could help increase fluorescence signals in the tumor, but in a different way: as Tat promoted tissue penetration and led to enhanced probe signals in all the organs (compared with non-modified silver nanoparticles), iron oxide nanoparticles contributed to increased accumulation of nanoparticles just in tumor except other organs, suggesting magnetism promoted tumor retention other than penetration. Taken together, it was proposed the dual functional nanovehicles worked in a two-step process: the as-prepared Tat-

FeAgNPs might firstly overcome the shear force from the blood stream and reach the target organs under external magnetic field. Then, surface modified TAT might further promote tissue penetration, thus could efficiently improve targeting efficiency. ICP-MS assay demonstrated that the tumor seized $6.7 \pm 2.4\%$ ID of the Tat-FeAgNPs, which was significantly higher than most of the previous reports. Anti-tumor assessment also demonstrated that Tat-FeAgNP-Dox displayed the most significant tumor-inhibiting effects among all the testing nanocarriers, showing a reduction of 29.6% in the SGR (specific growth rate) of tumor comparing with the PBS control ($P = 0.009$), while the other groups including AgNP-Dox, Tat-AgNP-Dox, and FeAgNP-Dox displayed no significant difference.

The sufficient on-site delivery by our dual functional system (Tat-FeAgNPs) in delivering doxorubicin and Cy5 to the xenograft tumors of mouse supported the hypothesis that enhanced EPR effect together with improved tissue/cell penetration would facilitate a substantially increased cancer drug delivery. However, our results reconfirmed the dilemma for the conventional nanovehicle-based drug delivery system. Since tumor in anatomically was not a preferential target for the circulating drug/nanovehicles as compared with other organs (liver, spleen, etc.), cancer drug vehicles should be more specifically designed with respect to the restrictive factors in systemic targeting delivery. Furthermore, as our system did not rely on specific binding with tumor cells but on externally applied magnet, it was reasonable to assume that Tat-FeAgNPs were apt to deliver loaded drugs/imaging reagents to any organs of the body where localized magnetic field was applied, which had been approved by enhanced brain delivery of intravenously given Tat-FeAgNP-Cy5 by attaching a magnet to the mouse brain. Therefore, Tat-FeAgNPs might serve as a multi-target delivery system in the future.

Acknowledgements

Great thanks are extended to Prof. Duxin Sun at College of Pharmacy, University of Michigan, for his instructive advice on paper organizing and writing. We also thank for the financial supports from National Key Research and Development Plan of China (2016YFE0119200) , the Young Elite Scientists Sponsorship Program by Tianjin (No. TJSQNTJ-2017-14) and National Natural Science Foundation of China (NSFC 81361140344, 21376164, 81402885, and 81373357).

Appendix A. Supplementary material

Supplementary data associated with this article can be found in the online version at https://doi.org/10.1016/j.apsb.2018.07.012.

References

1. Matsumura Y, Maeda H. A new concept for macromolecular therapeutics in cancer chemotherapy: mechanism of tumoritropic accumulation of proteins and the antitumor agent smancs. *Cancer Res* 1986;**46**:6387–92.
2. Kang L, Gao ZG, Huang W, Jin MJ, Wang QM. Nanocarrier-mediated co-delivery of chemotherapeutic drugs and gene agents for cancer treatment. *Acta Pharm Sin B* 2015;**5**:169–75.
3. Kratz F. A clinical update of using albumin as a drug vehicle—a commentary. *J Control Release* 2014;**190**:331–6.
4. Swierczewska M, Han H, Kim K, Park J, Lee S. Polysaccharide-based nanoparticles for theranostic nanomedicine. *Adv Drug Deliv Rev* 2016;**99**:70–84.
5. Duncan R, Vicent MJ. Polymer therapeutics-prospects for 21st century: the end of the beginning. *Adv Drug Deliv Rev* 2013;**65**:60–70.
6. Steichen SD, Caldorera-Moore M, Peppas NA. A review of current nanoparticle and targeting moieties for the delivery of cancer therapeutics. *Eur J Pharm Sci* 2013;**48**:416–27.
7. Kwon IK, Lee SC, Han B, Park K. Analysis on the current status of targeted drug delivery to tumors. *J Control Release* 2012;**164**:108–14.
8. Wilhelm S, Tavares AJ, Dai Q, Ohta S, Audet J, Dvorak HF, et al. Analysis of nanoparticle delivery to tumours. *Nat Rev Mater* 2016;**1**:16014.
9. Jain RK, Baxter LT. Mechanisms of heterogeneous distribution of monoclonal antibodies and other macromolecules in tumors: significance of elevated interstitial pressure. *Cancer Res* 1988;**48**:7022–32.
10. Liu E, Zhang M, Huang Y. Pharmacokinetics and pharmacodynamics (PK/PD) of bionanomaterials. In: Zhao Y, Shen Y, editors. *Biomedical Nanomaterials*. Weinheim: Wiley-VCH Verlag GmbH & Co. KGaA; 2016. p. 1–60.
11. Liu J, Zhao Y, Guo Q, Wang Z, Wang H, Yang Y, et al. Tat-modified nanosilver for combating multidrug-resistant cancer. *Biomaterials* 2012;**33**:6155–61.
12. Decuzzi P, Ferrari M. Design maps for nanoparticles targeting the diseased microvasculature. *Biomaterials* 2008;**29**:377–84.
13. Cao Q, Han X, Li L. Enhancement of the efficiency of magnetic targeting for drug delivery: development and evaluation of magnet system. *J Magn Magn Mater* 2011;**323**:1919–24.
14. Schwarze SR, Ho A, Vocero-Akbani A, Dowdy SF. *In vivo* protein transduction: delivery of a biologically active protein into the mouse. *Science* 1999;**285**:1569–72.
15. Eguchi A, Akuta T, Okuyama H, Senda T, Yokoi H, Inokuchi H, et al. Protein transduction domain of HIV-1 Tat protein promotes efficient delivery of DNA into mammalian cells. *J Biol Chem* 2001;**276**:26204–10.
16. Zhang J, Fu Y, Lakowicz JR. Enhanced förster resonance energy transfer (FRET) on a single metal particle. *J Phys Chem C* 2007;**111**:50–6.
17. Mehrara E, Forssell-Aronsson E, Bernhardt P. Objective assessment of tumour response to therapy based on tumour growth kinetics. *Br J Cancer* 2011;**105**:682–6.
18. Gomez-Roca C, Koscielny S, Ribrag V, Dromain C, Marzouk I, Bidault F, et al. Tumor growth rates and recist criteria in early drug development. *Eur J Cancer* 2011;**47**:2512–6.
19. Park J, Sun B, Yeo Y. Albumin-coated nanocrystals for carrier-free delivery of paclitaxel. *J Control Release* 2017;**263**:90–1.
20. Chiou JR, Lai BH, Hsu KC, Chen DH. One-pot green synthesis of silver/iron oxide composite nanoparticles for 4-nitrophenol reduction. *J Hazard Mater* 2013;**248**:394–400.
21. Ebrahimi N, Rasoul-Amini S, Niazi A, Erfani N, Moghadam A, Ebrahiminezhad A, et al. Cytotoxic and apoptotic effects of three types of silver-iron oxide binary hybrid nanoparticles. *Curr Pharm Biotechnol* 2016;**17**:1049–57.
22. Smolensky ED, Park HYE, Zhou Y, Rolla GA, Marjańska M, Botta M, et al. Scaling laws at the nanosize: the effect of particle size and shape on the magnetism and relaxivity of iron oxide nanoparticle contrast agents. *J Mater Chem B* 2013;**1**:2818–28.
23. Gu B, Chen Z, Llang L, McCarthy J, Schmitt J. Adsorption and desorption of natural organic matter on iron oxide: mechanisms and models. *Environ Sci Technol* 1994;**28**:38–46.
24. Gupta AK, Gupta M. Synthesis and surface engineering of iron oxide nanoparticles for biomedical applications. *Biomaterials* 2005;**26**:3995–4021.
25. Patakfalvi R, Virányi Z, Dékány I. Kinetics of silver nanoparticle growth in aqueous polymer solutions. *Colloid Polym Sci* 2004;**283**:299–305.
26. Filippo E, Serra A, Buccolieri A, Manno D. Green synthesis of silver nanoparticles with sucrose and maltose: morphological and structural characterization. *J Non-Cryst Solids* 2010;**356**:344–50.

27. Wang YXJ. Superparamagnetic iron oxide based MRI contrast agents: current status of clinical application. *Quant Imaging Med Surg* 2011;**1**:35–40.
28. Greenfield RS, Kaneko T, Daues A, Edson MA, Fitzgerald KA, Olech LJ, et al. Evaluation *in vitro* of adriamycin immunoconjugates synthesized using an acid-sensitive hydrazone linker. *Cancer Res* 1990;**50**:6600–7.
29. Braslawsky GR, Edson MA, Pearce W, Kaneko T, Greenfield RS. Antitumor activity of adriamycin (hydrazone-linked) immunoconjugates compared with free adriamycin and specificity of tumor cell killing. *Cancer Res* 1990;**50**:6608–14.
30. Kaneko T, Willner D, Monkovic I, Knipe JO, Braslawsky GR, Greenfield RS, et al. New hydrazone derivatives of adriamycin and their immunoconjugates—a correlation between acid stability and cytotoxicity. *Bioconjug Chem* 1991;**2**:133–41.
31. Lopez-Tobar E, Hernández Bn, Ghomi MSanchez-Cortes S. Stability of the disulfide bond in cystine adsorbed on silver and gold nanoparticles as evidenced by SERS data. *J Phys Chem C* 2013;**117**:1531–7.
32. Breshike CJ, Riskowski RA, Strouse GF. Leaving Förster resonance energy transfer behind: nanometal surface energy transfer predicts the size-enhanced energy coupling between a metal nanoparticle and an emitting dipole. *J Phys Chem C* 2013;**117**:23942–9.
33. Xiao Y, Hong H, Matson VZ, Javadi A, Xu W, Yang Y, et al. Gold nanorods conjugated with doxorubicin and cRGD for combined anticancer drug delivery and PET imaging. *Theranostics* 2012;**2**:757.
34. Rankin DW. CRC handbook of chemistry and physics, 89th edition, edited by David R. Lide. *Crystallogr Rev* 2009; **15**: 223–224.